J Adv Ceram

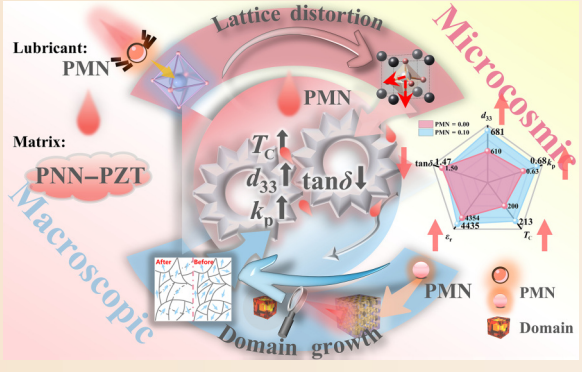
Research Article

$Pb(Mg_{1/3}Nb_{2/3})O_3$-induced oxygen octahedral distortions and domain growth for concurrent enhancement of multiple parameters in PNN–PZT

Zi'ao Xing[1,2,3], Wei Peng[1,2,4,✉], Chenming Gu[1,2,3], Zhengran Chen[1,2], Dongxu Cheng[1,2], Xiaorong Lu[1,2], Ruihong Liang[1,2,✉]

Cite this article: Xing Z, Peng W, Gu C, et al. *J Adv Ceram* 2026, **15**(5): 9221294. https://doi.org/10.26599/JAC.2026.9221294

ABSTRACT: Enhancing key parameters such as the piezoelectric coefficient (d_{33}), Curie temperature (T_C), electromechanical coupling coefficient (k_p), and dielectric loss (tanδ) is crucial for improving the overall performance of piezoelectric ceramics. However, the trade-off relationships among these parameters represent a significant challenge in this field. To address this issue, we propose a synergistic strategy that leverages atomic radius differences (Mg^{2+} and $Pb(Mg_{1/3}Nb_{2/3})O_3$) to induce lattice distortion and promote ferroelectric domain growth. This approach successfully achieves the simultaneous enhancement of multiple parameters in the $Pb(Ni_{1/3}Nb_{2/3})O_3$–$PbZrO_3$–$PbTiO_3$ system, resulting in excellent overall performance with d_{33} = 681 pC/N, inverse piezoelectric coefficient d_{33}* = 953 pm/V, T_C = 213 °C, k_p = 0.69, and tanδ = 1.47%. Rietveld refinement, Rayleigh analysis, and piezoresponse force microscopy (PFM) characterization confirm that the cooperative modulation of lattice distortion and domain growth is key to performance improvement. Additionally, the material demonstrates excellent thermal stability and high-temperature dielectric breakdown strength. This study provides a simple and effective strategy to overcome the antagonistic relationships among multiple parameters in piezoelectric ceramics.



KEYWORDS: lattice distortion; domain growth; simultaneous enhancement of multiple parameters; high-temperature stability

1 Introduction

Piezoelectric ceramics, as functional materials capable of converting mechanical energy into electrical energy and vice versa, play a critical role in electronic devices such as sensors, transducers, and actuators [1,2]. Among the various piezoelectric material systems, perovskite-structured oxides are one of the most extensively studied due to their exceptional piezoelectric tunability. The general formula for perovskite structures is ABO_3, where the B-site is typically occupied by transition metal ions that, together with oxygen, form [BO_6] octahedra. These octahedra are connected in a three-dimensional network through shared vertices, imparting a rich array of physicochemical properties to piezoelectric materials [3,4]. In a perfect perovskite structure, the high symmetry of the oxygen octahedra does not give rise to piezoelectricity. The piezoelectric effect fundamentally originates from the presence of noncentrosymmetric crystal structures, which lead to a relative displacement of the positive and negative charge centers, resulting in polarization. In other words, piezoelectricity arises from the displacement and distortion of nonideal oxygen octahedra symmetry centers, and the piezoelectric performance is closely linked to the extent of octahedral distortion [5–7].

From a chemical perspective, there are typically two approaches to improving the oxygen octahedral environment and inducing octahedral distortion [8]. The first is the Jahn–Teller (J–T) distortion, theoretically arising as a spontaneous behavior of the system seeking to minimize its total energy and achieve thermodynamic stability. To reach a more stable state, the structure undergoes geometric distortion, lifting degeneracy and resulting in a more stable electronic configuration [9–11]. The J–T effect is evident in the symmetry breaking within the oxygen

[1] State Key Laboratory of High Performance Ceramics, Shanghai Institute of Ceramics, Chinese Academy of Sciences, Shanghai 201899, China. [2] Key Laboratory of Inorganic Functional Materials and Devices, Shanghai Institute of Ceramics, Chinese Academy of Sciences, Shanghai 201800, China. [3] Center of Materials Science and Optoelectronics Engineering, University of Chinese Academy of Sciences, Beijing 100049, China. [4] Institute for Advanced Study, Shenzhen University, Shenzhen 518060, China.

✉ Corresponding authors. E-mail: W. Peng, pengwei@mail.sic.ac.cn; R. Liang, liangruihong@mail.sic.ac.cn

Received: January 29, 2026; Revised: April 3, 2026; Accepted: April 6, 2026

© The Author(s) 2026. This is an open access article under the terms of the Creative Commons Attribution 4.0 International License (CC BY 4.0, http://creativecommons.org/licenses/by/4.0/).

octahedra. This behavior is common in transition metal ions such as Fe^{3+}, Sc^{3+}, and Sb^{5+}, which possess a different valence state compared with the original B-site ions [12–14]. The incorporation of these dopants effectively alters the local electronic structure of the B-site, significantly influencing the piezoelectric properties of the material. The second approach to inducing octahedral distortion involves disrupting structural symmetry through the mismatch in ionic radii. When ions with significantly different radii substitute for the A or B-sites in the perovskite structure, the oxygen octahedra expand or contract due to differences in ionic radii and electronegativity (Fig. 1), leading to a reduction in octahedral symmetry. Examples of such ions include Sr^{2+}, Ce^{3+}, and Ta^{5+} [15–19]. However, A-site doping typically results in a significant reduction in Curie temperature (T_C) in piezoelectric ceramics. Therefore, utilizing B-site ions to induce octahedral distortion while improving the overall piezoelectric performance and maintaining/enhancing T_C may be an ideal strategy.

The alteration of B–O bond interactions (lattice distortion) is reflected in its influence on the ferroelectric domain structure. In the design of piezoelectric materials, ferroelectric domains, as key macroscopic structural units, play a critical role, with their size (microdomains and nanodomains) and morphology (90° and 180° domains) directly determining the macroscopic piezoelectric response [20–24]. Previous studies have demonstrated that introducing partially polar nanoregions (PNRs) into piezoelectric materials can induce a dynamic competition between interfacial energy and matrix free energy, making polarization highly sensitive to external electric fields. This metastable state facilitates the reorientation of ferroelectric domains, significantly improving the piezoelectric performance [25,26], as reported by Li *et al.* [27] for Sm–$Pb(Mg_{1/3}Nb_{2/3})O_3$–$PbTiO_3$ (Sm–PMN–PT) and Yan *et al.* [28] for Fe–$Pb(Ni_{1/3}Nb_{2/3})O_3$–$PbHfO_3$-$PbTiO_3$ (Fe–PNN–PHT). Although this method of disrupting the long-range order of ferroelectric domains can achieve an exceptionally high piezoelectric coefficient (d_{33}), it often leads to a loss in other properties (e.g., T_C, k_p, and tanδ), making it challenging to obtain piezoelectric ceramics with balanced overall performance. Additionally, an excessive number of small domains may increase the domain wall density, leading to strong domain wall pinning effects that undermine the piezoelectric performance [29]. Therefore, under conditions that ensure a certain content of small domains, promoting domain growth while alleviating the domain wall pinning effect can significantly improve the overall performance of piezoelectric ceramics (Fig. 1).

To date, strategies that utilize differences in ionic radius to induce oxygen octahedral distortion and promote ferroelectric domain growth to enhance T_C and concurrently improve d_{33}, k_p, and tanδ remain limited [30–32]. In this work, building on our previous research, we selected the $Pb(Ni_{1/3}Nb_{2/3})O_3$–$PbZrO_3$–$PbTiO_3$ (PNN–PZT) system as the matrix material and exploited the ionic radius differences between Mg^{2+} and Ni^{2+} to induce lattice distortion while simultaneously promoting ferroelectric domain growth (Fig. 1). This approach enabled the simultaneous enhancement of multiple parameters, including d_{33}, inverse piezoelectric coefficient d_{33}*, and k_p, under conditions of elevated T_C. Notably, we achieved excellent overall performance for the PNN–PZT system at high T_C, with values of d_{33} = 681 pC/N, d_{33}* = 953 pm/V, T_C = 213 °C, k_p = 0.69, tanδ = 1.47%, and H = 14.14% (@ 1 kV/mm, H: maximum hysteresis of unipolar strain–electric field (S–E).

2 Experiment and characterization

The xPb$(Mg_{1/3}Nb_{2/3})O_3$–(0.38–x)Pb$(Ni_{1/3}Nb_{2/3})O_3$–0.24$PbZrO_3$–0.38$PbTiO_3$ ceramics (abbreviated as xPMN–(0.38–x)PNN–PZT, where x = 0.00, 0.05, 0.10, 0.15, and 0.20) were synthesized using a high-temperature solid-state method. Pb_3O_4 (99.76%), MgO (99.99%), NiO (99.90%), Nb_2O_5 (99.99%), ZrO_2 (99.76%), and TiO_2 (99.62%) were weighed according to stoichiometric ratios. To compensate for PbO volatilization during high-temperature sintering, an excess of 1.5 mol% Pb_3O_4 was added. The materials were then mixed using a planetary ball mill for 4 h with ethanol as the medium. After drying in an oven, the mixture was pre-synthesized at 850 °C for 2 h, followed by secondary planetary ball milling for 6 h. The dried powder was granulated with 5 wt% polyvinyl alcohol (PVA) and pressed into discs with a diameter of 13 mm and a thickness of 2 mm. After a plasticizer removal process at 600 °C for 2 h, the samples were sintered at 1250 °C for 2 h to achieve high-density ceramics.

After sintering, the samples underwent ultrasonic cleaning in gasoline, detergent, and anhydrous ethanol for 10 min each, followed by drying to remove surface contaminants. Sintered ceramic samples were ground into powder using an agate mortar and then sieved through a 200-mesh screen to ensure uniform particle size. The phase composition of the xPMN–(0.38–x) PNN–PZT ceramics was investigated via an X-ray diffractometer (XRD; Rigaku RAX-10, Japan), with Rietveld refinement performed using FullProf software. The cleaning procedure was identical to that used for XRD sample preparation. Ceramics were subjected to successive rough polishing stages using 800-, 1500-, and 3000-mesh millstones. Fine polishing was carried out with a polishing cloth, resulting in a mirror-like surface (notably, the durations for rough and fine polishing are not fixed, as the process only needs to achieve a mirror-like finish). The second ultrasonic treatment in gasoline, detergent, and anhydrous ethanol for 10 min was performed, followed by drying to eliminate any residual surface contaminants. To reveal the grain boundaries, polished samples were heated to 1050 °C for 30 min, inducing thermal corrosion on the ceramic surfaces. Their microstructure was examined by a scanning electron microscope (SEM; SU8220, HITACHI, Japan). Prior to imaging, the samples were sputtered with a thin layer of carbon to mitigate charge accumulation. Piezoelectric ceramics were fabricated into 1 mm thick discs with both surfaces coated with silver electrodes, which were prepared by annealing at 750 °C for 30 min. Samples were then polarized under an electric field of 4.0 kV/mm for 30 min and allowed to

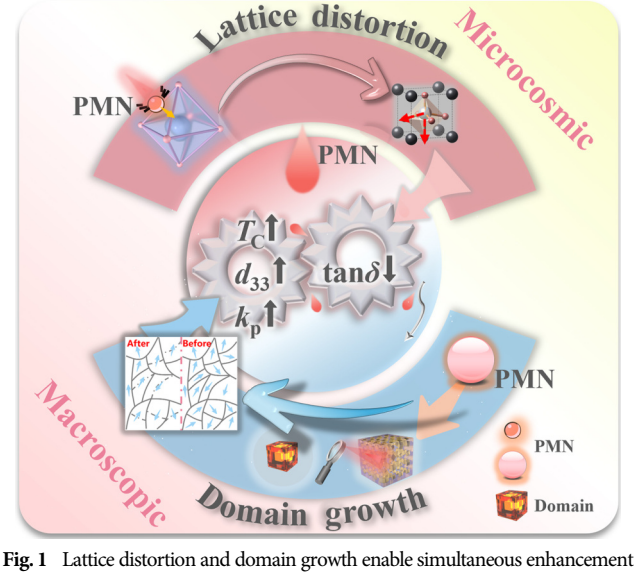


Fig. 1 Lattice distortion and domain growth enable simultaneous enhancement of multiple parameters.

rest for 24 h to ensure complete discharge. The d_{33} was measured using a quasi-static d_{33} meter (ZJ-3A, Institute of Acoustics, Chinese Academy of Sciences). Dielectric properties, including the dielectric constant (ε_r) and tanδ, were assessed using an impedance analyzer (Agilent 4294A, Agilent Technologies, Japan). Polarization–electric field (*P*–*E*) and *S*–*E* loops of the 1 mm sample were recorded using a ferroelectric tester (aixACCT Systems GmbH, Germany, @ 10 Hz) equipped with an optical displacement sensor. For piezoresponse force microscopy (PFM) characterization, the sample preparation followed the same procedures as SEM polishing, but without thermal corrosion. A silver paste electrode (Leit Silber 200 Silver Paint, Ted Pella, USA) was applied to the edge of the upper surface to establish electrical connectivity. The domain structure was analyzed using a piezoresponse force microscope (Vero ES, Asylum Research, UK, @ 2 V).

3 Results and discussion

As mentioned previously, the [BO_6] octahedra significantly influence the overall performance of piezoelectric ceramics. Therefore, Fig. 2 systematically examines the effect of varying PMN content (x = 0.00, 0.05, 0.10, 0.15, and 0.20) on the crystal structure of xPMN–(0.38–x)PNN–PZT piezoelectric ceramics. Figure 2(a) presents the XRD patterns of xPMN–(0.38–x) PNN–PZT ceramics over the 10°–80° range. All samples exhibit a pure perovskite structure, with no discernible secondary phases, indicating that Mg^{2+} is successfully incorporated into the lattice, forming a solid solution with PNN–PZT. Additionally, near 2θ = 45°, the (200) peak exhibits noticeable splitting, suggesting that the ceramics predominantly consist of the tetragonal phase (T-phase, *P4mm*). The diffraction angles (Fig. S1(a) in the Electronic Supplementary Material (ESM)) corresponding to the characteristic peaks (002) and (200) of the T-phase are primarily observed. As x increases, both tetragonal peaks shift slightly toward lower angles. According to Bragg's law, the ionic radius of Mg^{2+} ($r_{Mg^{2+}}$ = 0.72 Å) is slightly larger than that of Ni^{2+} ($r_{Ni^{2+}}$ = 0.69 Å), suggesting that the incorporation of Mg^{2+} may lead to slight lattice expansion. This results in an increase in the interplanar spacing, thereby causing a slight reduction in the diffraction angle.

To further investigate the origin of the enhanced piezoelectricity, Rietveld refinement of the XRD data was performed using FullProf software [33]. Figure 2(b) shows the refinement results for ceramics with varying PMN content. All results are within reasonable error limits, confirming the high reliability of the refinement outcomes. The relative phase content of the tetragonal phase (T-phase, *P4mm*) and rhombohedral phase (R-phase, *R3m*), along with the corresponding lattice parameters, is provided in Table S1 in the ESM. As the PMN content increases, the phase structure transitions from being predominantly T phase to a coexistence of T and R phases, indicating that the material approaches the morphotropic phase

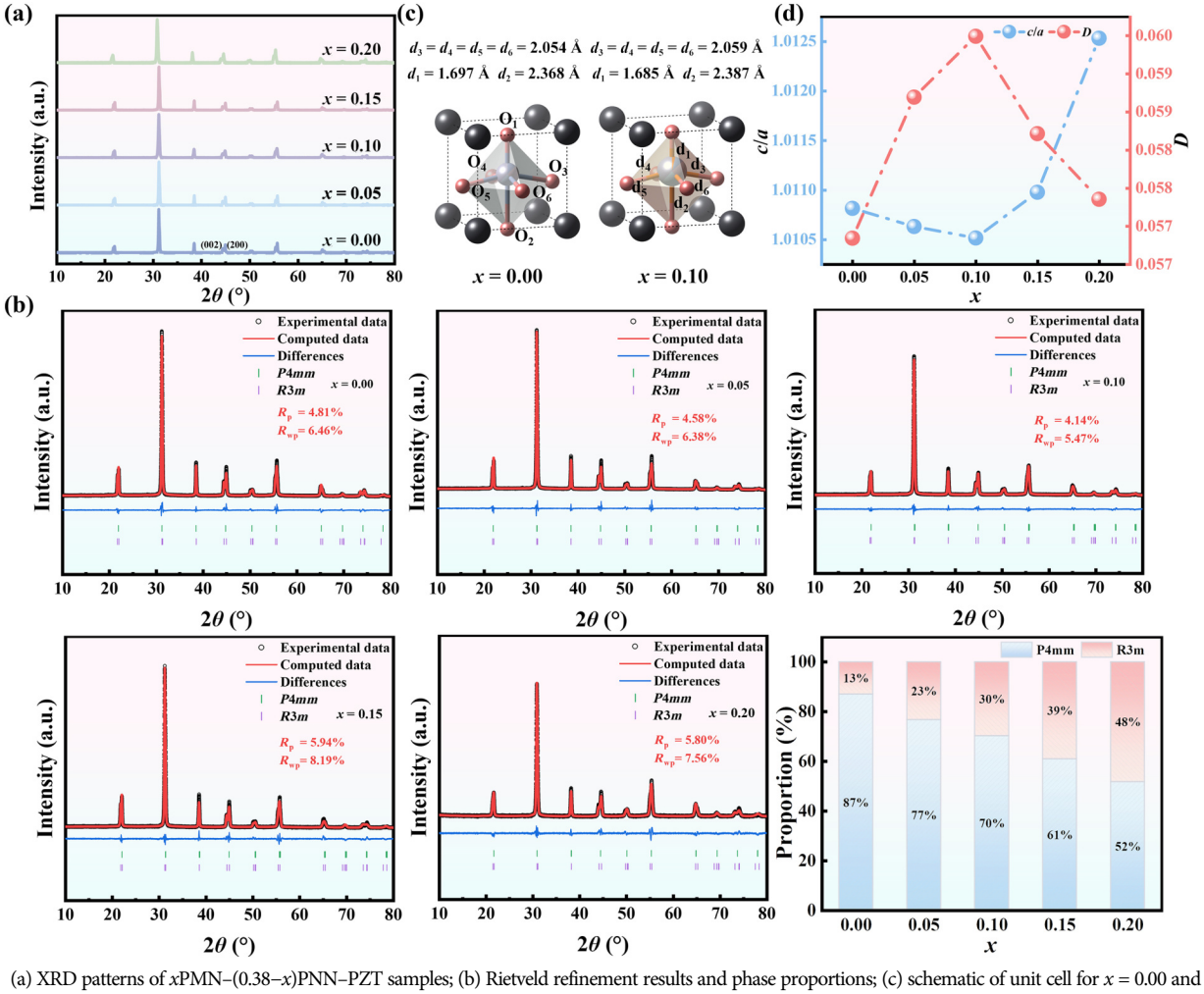


Fig. 2 (a) XRD patterns of xPMN–(0.38–x)PNN–PZT samples; (b) Rietveld refinement results and phase proportions; (c) schematic of unit cell for x = 0.00 and 0.10; (d) c/a ratio and D values for all samples.

boundary (MPB). It is generally accepted that the coexistence of phases near the MPB enhances the polarization vector and reduces the domain switching energy barrier, thereby improving the piezoelectric performance [34].

Based on the ionic radii and refined unit cell parameters, a schematic of the Pb_8O_6 unit cell is constructed in Fig. 2(c). This unit cell contains four Pb ions and one oxygen ion at the face center of each face. At the center of the unit cell is the [BO_6] octahedron, formed by B-site ions (Mg^{2+}, Ni^{2+}, Zr^{4+}, Ti^{4+}, and Nb^{5+}). The oxygen atoms at the upper and lower vertices of the octahedron are labeled O_1 and O_2, respectively, while the four oxygen atoms in the middle plane are denoted as O_3–O_6. The corresponding B–O bond lengths are represented as d_i. Figure 2(c) compares the variation in B–O bond lengths for x = 0.00 and x = 0.10, showing that the bond lengths increase with the introduction of Mg^{2+}, which is consistent with the induced lattice expansion. Notably, for x = 0.00 and 0.10, d_2 and d_1 exhibit significant changes, suggesting the possible occurrence of substantial lattice distortion. Furthermore, by statistically analyzing the changes in B–O bond lengths for different compositions, the octahedral distortion degree (D, Eq. (1)) and the crystal lattice parameters c/a ratio were calculated to evaluate the specific structural distortion behavior [35]:

$$D = \frac{1}{6}\sum_{i=1}^{6}\frac{|d_i - d_{avg}|}{d_{avg}} \quad (1)$$

where d_i represents any individual B–O bond length, d_{avg} denotes the average B–O bond length, and D refers to the degree of distortion of the BO_6 octahedron.

Figure 2(d) illustrates the relationship between the c/a ratio and the D under varying PMN content. As shown, with increasing PMN content, the lattice distortion initially increases and then gradually decreases, which is consistent with the trend observed in d_2/d_1 (Fig. S1(b) in the ESM). In contrast, the c/a ratio exhibits the opposite trend. The incorporation of PMN causes the unit cell to expand, in accordance with the electronegativity rule. Additionally, both the c- and a-axis unit cell parameters increase, with the a-axis experiencing a slightly larger change than the c-axis. This results in a decrease in the c/a ratio at early stages (Table S1 in the ESM). This suggests that the introduction of an optimal amount of PMN leads to significant unit cell distortion, which is beneficial for enhancing the piezoelectric properties of the ceramics.

It is well known that the piezoelectric performance of ceramics is not only influenced by lattice distortion but is also limited by factors such as grain size and ferroelectric domain structure. According to the studies by Qiao *et al.* [23] and Shi *et al.* [35], a reduction in B–O bond length enhances local polarity and disrupts long-range ferroelectric domain ordering, thereby promoting the formation of PNRs. Consequently, it can be reasonably inferred that an increase in the B–O bond length may facilitate the growth of ferroelectric domains and lead to the formation of larger macroscopic domain regions. Since the morphology of ferroelectric domains is closely related to the piezoelectric properties of ceramics, PFM was employed to directly characterize the changes in ferroelectric domain structure for the different samples to further investigate the influence of PMN on domain formation.

The amplitude and phase images for different PMN samples (x = 0.00, 0.10, and 0.20) are presented in Figs. 3(a)–3(c) (height images, Figs. S2(a)–S2(c) in the ESM). It is evident that as x increases, significant changes in the domain structure are observed. For samples with x = 0.00 and x = 0.10, the domain structure exhibits an irregular, diffuse island-like structure, indicating a high degree of disorder. The corresponding phase images reveal that with increasing x, the domain size notably increases. At x = 0.10, the ferroelectric domains still display a local disorder characteristic, retaining some small domain structures. Studies have shown that increasing the domain size can help mitigate the domain-wall pinning effect [36]. This suggests that a moderate addition of PMN can reduce the domain-wall density by promoting domain growth while still maintaining local disorder, thereby enhancing the piezoelectric properties. With a further increase in x, distinct 180° stripe domains appear in the sample (Fig. 3(c)), and long-range order further develops, which may lead to a subsequent decline in piezoelectric performance. Additionally, the changes in average amplitude reflect the evolution of piezoelectric performance. It is generally accepted that amplitude is positively correlated with piezoelectricity [37]. The sample with x = 0.10 exhibits the highest average amplitude, consistent with its optimal piezoelectric properties.

Moreover, the surface morphology and particle size distribution of the corresponding compositions are shown in Figs. 3(h)–3(j) (detailed SEM, Fig. S3 in the ESM). All samples underwent thermal etching treatment. The ceramic microstructure is dense with few pores, and no significant abnormal grain growth or secondary phases were observed. As x increases, the grain size first increases and then decreases. When x = 0.10, the average grain size (AGS) reaches its maximum at 3.50 μm. The increase in grain size implies a reduction in the number of grain boundaries, which helps alleviate the intergranular constraints, thereby enhancing the piezoelectric performance [38]. However, when x = 0.20, the high PMN content inhibits grain growth, resulting in a decline in piezoelectric properties. This phenomenon has also been observed in the studies of Peng *et al.* [39] and Yan *et al.* [40]. Consequently, this suggests that both the lattice distortion and macrostructural factors jointly govern the piezoelectric performance of the ceramics.

Additionally, Fig. 4 depicts the energy-dispersive X-ray spectroscopy (EDS) mappings of the 0.10PMN–0.28PNN–PZT ceramic sample, while the corresponding EDS spectrum and full elemental distribution are provided in Figs. S1(c) and S3(f) in the ESM, respectively. As shown in Fig. 4(b), all major elements (Pb, Mg, Ni, Nb, Zr, and Ti) are evenly distributed within the grains, with no noticeable elemental enrichment or segregation observed. This result indicates that the elements form a well-integrated solid solution within the lattice, consistent with the conclusions drawn from the XRD analysis [41,42].

As a typical relaxor ferroelectric, the introduction of PMN inevitably influences the dielectric properties of the ceramics. The dielectric performance of xPMN–(0.38–x)PNN–PZT ceramics was measured from room temperature to 300 °C at different frequencies (Fig. S4 in the ESM). With increasing x content, the variation in tanδ with temperature and frequency gradually decreases, with more pronounced changes observed in the high-temperature region. This trend indicates a reduced temperature dependence of the sample, leading to enhanced thermal stability. Meanwhile, the temperature corresponding to the maximum dielectric constant (T_m) shows a stronger frequency dependence. To further explore the relaxor characteristics of different ceramic samples, the temperature dependence of the relative dielectric constant was derived based on the Curie–Weiss law (Eq. (S1) and Fig. S4(f) in the ESM), revealing an enhancement in the relaxor behavior as x increases. This enhanced relaxor behavior is also reflected in changes in domain structure. Figure 5(a) presents the

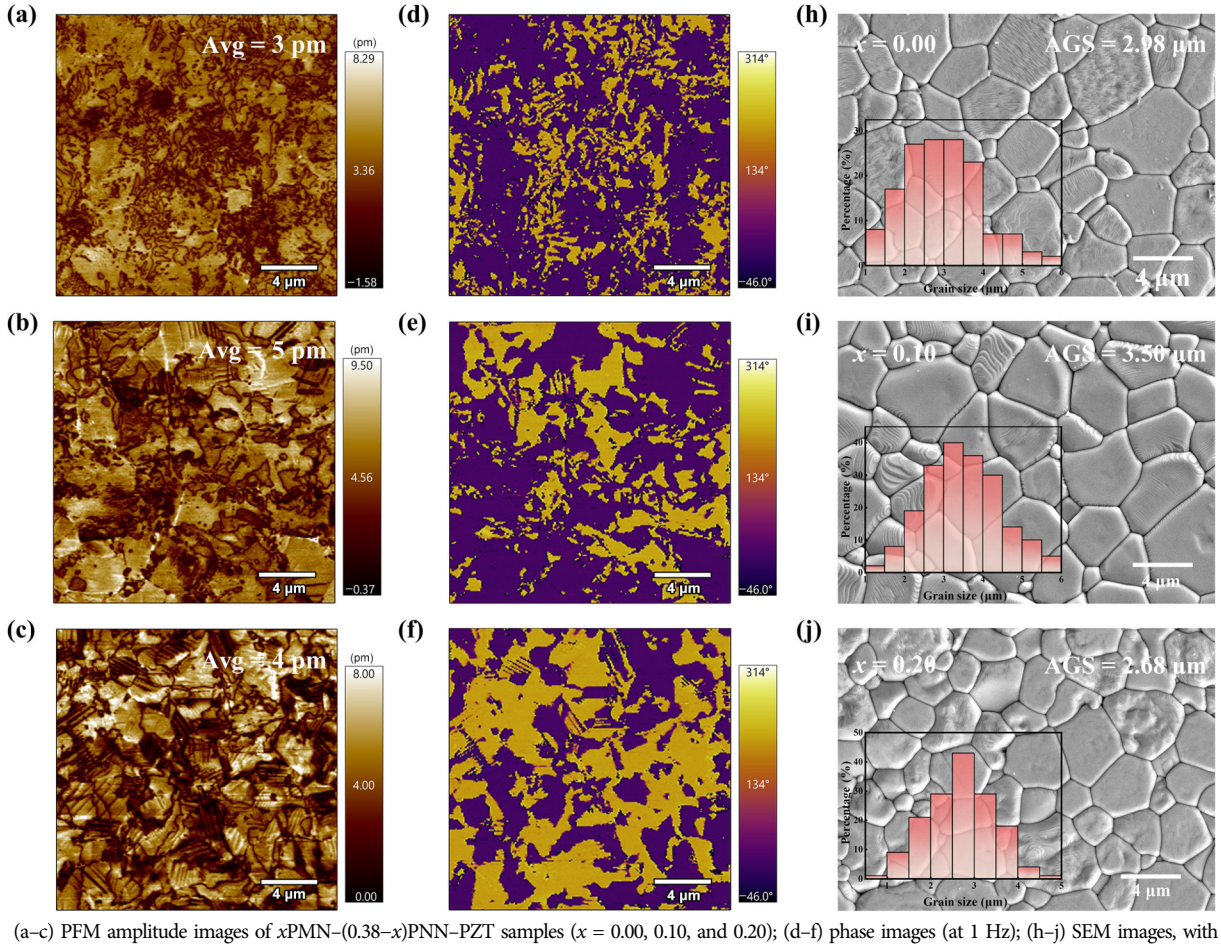


Fig. 3 (a–c) PFM amplitude images of *x*PMN–(0.38–*x*)PNN–PZT samples (x = 0.00, 0.10, and 0.20); (d–f) phase images (at 1 Hz); (h–j) SEM images, with insets showing grain size statistics.

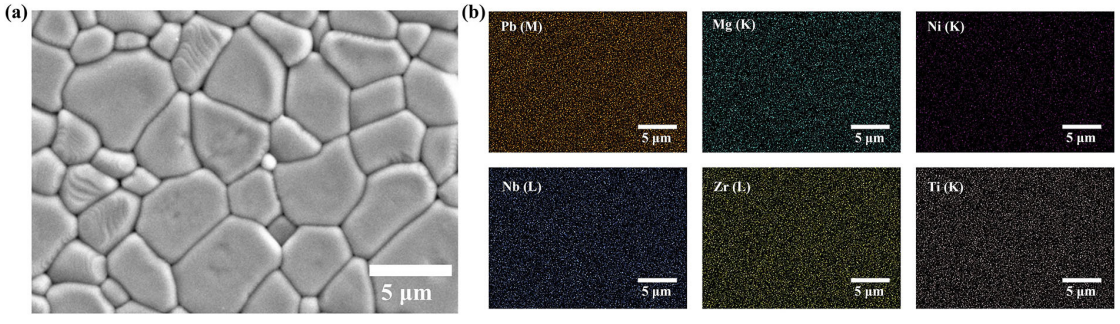


Fig. 4 (a) SEM images of *x*PMN–(0.38–*x*)PNN–PZT (x = 0.10) sample and (b) EDS mappings of *x*PMN–(0.38–*x*)PNN–PZT (x = 0.10) sample.

temperature-dependent dielectric constant of *x*PMN–(0.38–*x*)PNN–PZT ceramics at a frequency of 1 kHz. It is evident that with increasing x, the dielectric peak height increases, reaching a maximum at x = 0.15, after which it rapidly decreases. Furthermore, no distinct phase transition peak is observed below T_m, indicating the excellent temperature stability of the system.

The phase transition process of relaxor ferroelectrics typically spans a broad temperature range, with T_m often regarded as their characteristic T_C [58]. Figure 5(b) summarizes the T_C, d_{33}, and k_p of different ceramic samples, revealing a general upward trend in these parameters as the PMN content increases. Specifically, d_{33} and k_p reach their peaks at x = 0.10 and x = 0.15, respectively. Meanwhile, multiple parameters, including d_{33}, k_p, T_C, ε_r, and tanδ for the ceramic samples at x = 0.00 and x = 0.10, are primarily compared in Fig. 5(c) (Fig. S5 in the ESM, Table 1, and Eq. (S2) in the ESM). The results demonstrate that appropriate incorporation of PMN not only reduces tanδ but also enhances the other parameters simultaneously [41,59,60].

From a microscopic perspective, the synergistic improvement of these parameters is closely linked to the lattice distortion induced by the incorporation of PMN. The difference in B-site ion radii triggers lattice distortion, which in turn enhances the polarization response and contributes to improved piezoelectric properties. Furthermore, the addition of PMN promotes the favorable growth of ferroelectric domains, weakening domain wall pinning effects and thereby increasing k_p, while simultaneously reducing tanδ. These trends are consistent with the aforementioned findings (Fig. 2(d) and 3(a)–3(f)). Therefore, it can be concluded that lattice distortion induced by ion radius differences, coupled with the suppression of domain wall pinning

effects, is an effective strategy for achieving a simultaneous enhancement of multiple parameters in piezoelectric ceramics, particularly under conditions that increase the T_C.

In the PNN–PZT system, piezoelectric ceramics with high d_{33} are typically associated with a significant decrease in T_C. To more comprehensively showcase the excellent performance of PMN–PNN–PZT piezoelectric ceramics, Figs. 5(d) and 5(e) summarize the T_C–d_{33} and T_C–k_p relationships of PNN–PZT-based ceramics reported in recent studies. As shown, PMN–PNN–PZT ceramics exhibit outstanding performance (d_{33} = 681 pC/N, k_p = 0.69) at high T_C, achieving excellent performance at a similar T_C. This demonstrates that the incorporation of PMN effectively overcomes the trade-off between high overall performance and high T_C, highlighting its potential for applications in high-temperature and high-piezoelectric environments.

The piezoelectric performance of ceramics primarily arises from two factors: (i) lattice distortion as the major intrinsic contribution and (ii) domain switching and related behaviors as extrinsic contributions [61]. To further analyze the relationship between intrinsic and extrinsic contributions induced by PMN, we employed the Rayleigh model to quantify the intrinsic and extrinsic contributions of different samples, aiming to reveal the underlying mechanisms behind the enhancement of their piezoelectric properties. The specific expression of the Rayleigh model is given by Eqs. (2)–(5) [62]:

$$P(E_0) = (\varepsilon_{init} + \alpha E_0) E_0 \tag{2}$$

$$P(E) = (\varepsilon_{init} + \alpha E_0) E_0 \pm \alpha \left(E_0^2 - E^2\right)/2 \tag{3}$$

$$\varepsilon^* = \varepsilon_{init} + \alpha E_0 \tag{4}$$

$$\varepsilon^* = (P_{max} - P_{min})/2E_0 \tag{5}$$

where E_0 and $P(E_0)$ represent the applied electric field and the polarization intensity of the sample under the corresponding field strength, respectively. Typically, $E_0 \ll E_c$ (E_c is the coercive field), and under E_0, no new domains are formed, resulting in linear Rayleigh behavior. ε_{init} denotes the intrinsic contribution, including lattice distortion and reversible domain wall motion, although the latter contribution is minimal and therefore can be neglected. α is the slope of ε^* with respect to E_0, representing the extrinsic contribution arising from irreversible ferroelectric domain switching. Additionally, ε^* is calculated by dividing the difference between the positive and negative peaks under different electric fields E_0 by twice the applied field (Eq. (5)).

The fitting results of ε^* versus E_0 are shown in Fig. 6(a), where the linear behavior indicates that Rayleigh analysis is applicable to the PMN–PNN–PZT ceramic system. The corresponding trends of ε_{init} and α as a function of x are shown in Fig. 6(b). As the PMN content increases, both ε_{init} and α initially rise before decreasing. Notably, ε_{init} reaches its maximum at x = 0.10, while α peaks at x = 0.15. As previously mentioned, ε_{init} is associated with intrinsic lattice distortion, which confirms that the ceramic samples at x = 0.10 exhibit stronger lattice distortion. The enhancement in α primarily arises from the appropriate domain growth, which weakens the pinning effect between domain walls. However, excessive domain growth leads to difficulty in domain switching, resulting in a decrease in piezoelectric performance, as reflected by the reduction in α when x > 0.15 (Figs. 3, 5, and 6(c)). Therefore, the simultaneous enhancement of multiple parameters in PMN–PNN–PZT can be attributed to the combined contributions of enhanced intrinsic lattice distortion and weakened domain wall pinning effects, aligning with the initial material design strategy.

Figures 7(a)–7(d) depict the P–E loops, bipolar S–E loops, and the corresponding domain reversal current peaks (I–E) of PMN–PNN–PZT ceramics at room temperature. All samples exhibit saturated P–E and S–E curves, confirming the typical ferroelectric behavior of the ceramics. As x increases, the remanent polarization (P_r) increases from 30.86 to 35.48 μC/cm^2 (x = 0.15). The rise in P_r favors the achievement of higher k_p performance (Eq. (6)). For d_{33}, it is dependent on ε_r and P_r (Eq. (7)). Thus, although the P_r is slightly lower at x = 0.10, the higher ε_r results in the optimal d_{33} (Table 1).

We further extract the E_c and total bipolar strain (S_{tot}) for each composition, as illustrated in Fig. 7(c). As shown, the introduction of PMN reduces the E_c while significantly enhancing the bipolar strain (x = 0.10). This is mainly attributed to the weakening of the domain wall pinning effect, reducing the energy barrier for domain switching, which facilitates polarization and reorientation

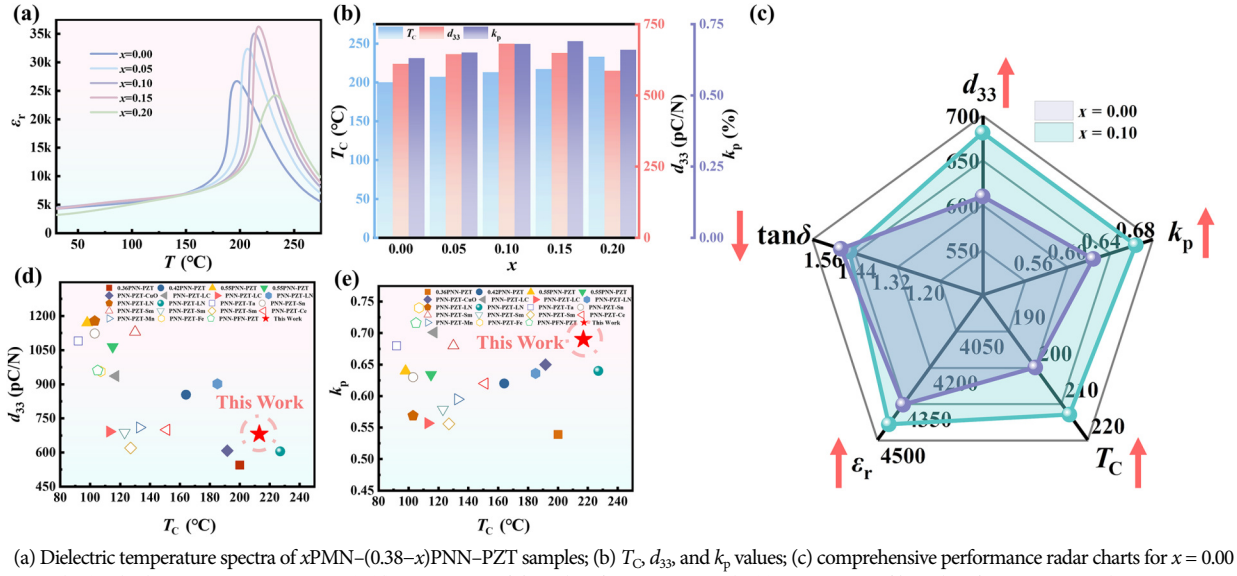


Fig. 5 (a) Dielectric temperature spectra of xPMN–(0.38–x)PNN–PZT samples; (b) T_C, d_{33}, and k_p values; (c) comprehensive performance radar charts for x = 0.00 and x = 0.10 samples (multiple parameter improvement); (d) comparison of d_{33} and T_C for x = 0.10 sample; (e) comparison of k_p and T_C for x = 0.15 sample [39,43–57].

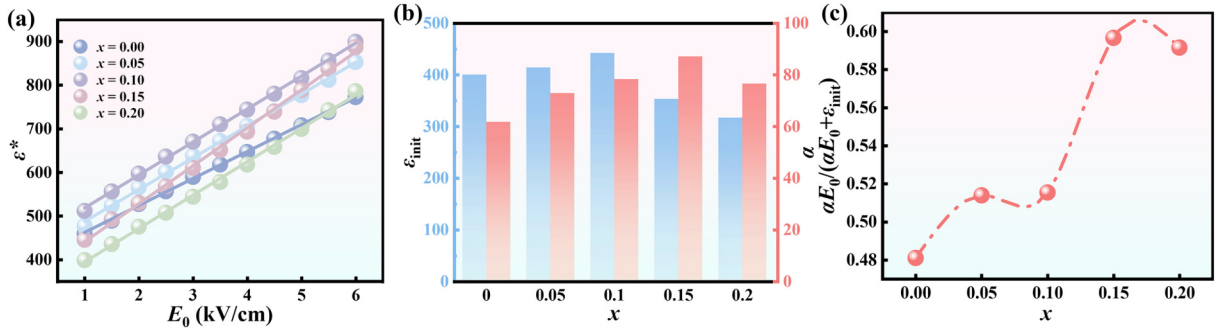


Fig. 6 (a) Electric field-dependent dielectric constant (ε^*–E) of xPMN–(0.38–x)PNN–PZT samples; (b) variation in ε_{init} and α; (c) variation in $\alpha E_0/(\alpha E_0+\varepsilon_{init})$ (E_0 = 6 kV/cm).

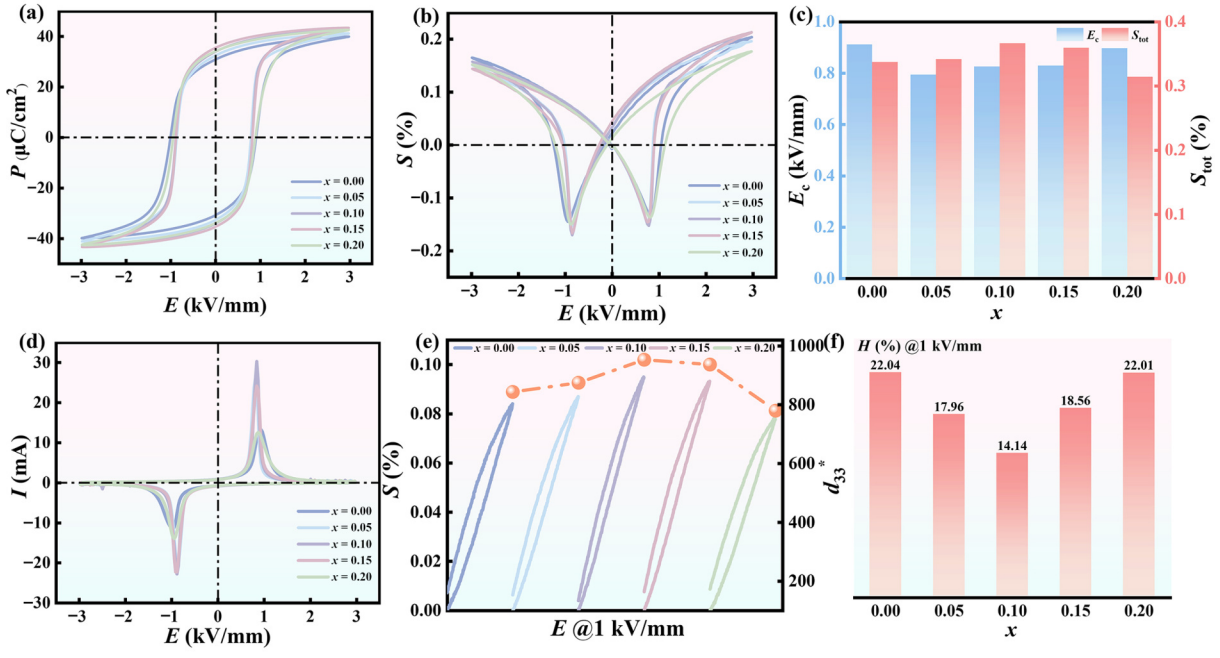


Fig. 7 (a) P–E hysteresis loops of xPMN–(0.38–x)PNN–PZT samples; (b) bipolar S–E loops; (c) summary of E_c and S_{tot} performance at 3 kV/mm, room temperature; (d) I–E loops; (e) unipolar S–E loops; (f) unipolar strain hysteresis at 1 kV/mm, room temperature.

Table 1 Performance summary of xPMN–(0.38–x)PNN–PZT

Performance	PMN content (x)				
	0.00	0.05	0.10	0.15	0.20
d_{33} (pC/N)	610	644	681	649	586
ε_r	4354	4400	4435	4134	3681
tanδ (%)	1.50	1.39	1.47	1.51	1.57
k_p	0.63	0.65	0.68	0.69	0.67
T_C (°C)	200	207	213	217	233

of the ferroelectric domains. This phenomenon is also reflected in the I–E curves (Fig. 7(d)), where the domain reversal current peak sharpens with increasing PMN content, indicating enhanced consistency in domain switching. However, it is important to note that when the PMN content is too high, grain growth is hindered, and the pinning effect at grain boundaries is amplified, making domain switching more difficult, which is reflected in the overall degradation of performance.

$$k_p = 2\left[\frac{2\varepsilon_{33}^T}{(1-\sigma)\,S_{11}^E g_{31}}\right]^{\frac{1}{2}} P_r \tag{6}$$

where ε_{33}^T denotes the free dielectric constant; σ is Poisson's ratio; S_{11}^E refers to the elastic compliance under short-circuit conditions; g_{31} represents the piezoelectric voltage constant.

$$d_{33} = 2Q\varepsilon_r P_r \tag{7}$$

where Q is the electrostrictive coefficient; ε_r denotes the relative permittivity; P_r represents the remanent polarization.

$$d_{33}^* = S_{max}/E_{max} \tag{8}$$

where S_{max} denotes the corresponding unipolar strain at the maximum voltage and E_{max} represents the maximum electric field strength.

清華大学出版社 Tsinghua University Press | SciOpen

$$H = \Delta S_{max}/S_{max} \quad (9)$$

where ΔS_{max} is defined as the maximum difference in unipolar strain and S_{max} represents the maximum unipolar strain corresponding to E_{max}.

Moreover, PMN–PNN–PZT ceramics exhibit high strain sensitivity under low electric fields. Figure 7(e) illustrates the unipolar strain performance of the ceramic samples under a field of 1 kV/mm. As x increases, the unipolar strain first increases and then decreases. The corresponding d_{33}* (Eq. (8)) is calculated from the unipolar strain, reaching a maximum value of 953 pm/V at x = 0.10. At the same time, this system demonstrates minimal strain hysteresis (H, Eq. (9), Fig. 7(f)). Typically, strain hysteresis is closely related to the domain structure of piezoelectric ceramics. This phenomenon may arise from the addition of PMN, which effectively weakens the domain wall pinning effect while maintaining a small domain size, allowing the ferroelectric domains to respond quickly to external field stimuli and undergo corresponding flipping [63]. From an energy perspective, the design of the MPB (T and R phases) also places the material in a metastable state. This metastability makes the polarization vector highly sensitive to the external electric field, facilitating polarization rotation and the reorientation of ferroelectric domains, leading to faster strain responses [64].

Temperature stability is a key performance indicator for piezoelectric ceramics. Therefore, a systematic evaluation of the temperature stability was conducted for the optimal composition (x = 0.10). The ferroelectric and bipolar strain behaviors of the ceramic samples are depicted in Figs. 8(a) and 8(b), respectively. As the temperature increases, the ferroelectric domain activity enhances, leading to a reduction in the energy barrier for domain switching under the same electric field, which manifests as a decrease in the E_c with rising temperature. Additionally, the domain switching current in the I–E curve (Fig. S6(a) in the ESM) gradually narrows, indicating that elevated temperatures improve the consistency of domain switching, making it easier at higher temperatures. Figure S6(b) in the ESM summarizes the variation in E_c and P_r with temperature. Despite the significant decrease in E_c with increasing temperature, the sample did not undergo breakdown, demonstrating excellent high-temperature breakdown resistance. At 160 °C (> 2/3T_C), the sample still retains a high P_r. This behavior is closely related to domain size control, as the presence of larger domains enhances performance stability at high temperatures. These characteristics are also reflected in the bipolar strain behavior shown in Fig. 8(b). Even near T_C, the sample maintains significant bipolar strain, further confirming the outstanding temperature stability of the ceramics.

The temperature-dependent unipolar S–E of the x = 0.10 sample under electric fields of 1 and 2 kV/mm are shown in Figs. 8(c) and 8(d), respectively. As previously noted, the energy barrier for domain reversal significantly decreases with temperature. However, due to the retention of a certain number of small domains, minor temperature fluctuations at the beginning of heating lead to a marked increase in unipolar strain. Furthermore, the unipolar strain of the x = 0.10 sample exhibits a slight decreasing trend as the temperature rises, a phenomenon commonly observed in previous studies [38,65,66], which may be related to its small domain size. Nevertheless, the coexistence of larger ferroelectric domains in the sample provides robust temperature stability, ensuring that the unipolar strain under different field strengths (1 and 2 kV/mm) only decreases by 0.020 and 0.026 up to 160 °C. Furthermore, the corresponding d_{33}* at different temperatures and corresponding electric fields are shown in Fig. 8(e). The results demonstrate that d_{33}* remains stable above 800 pm/V throughout the entire temperature range, further demonstrating the excellent temperature stability of the ferroelectric properties in this system.

Generally, k_p is more sensitive to temperature variations than

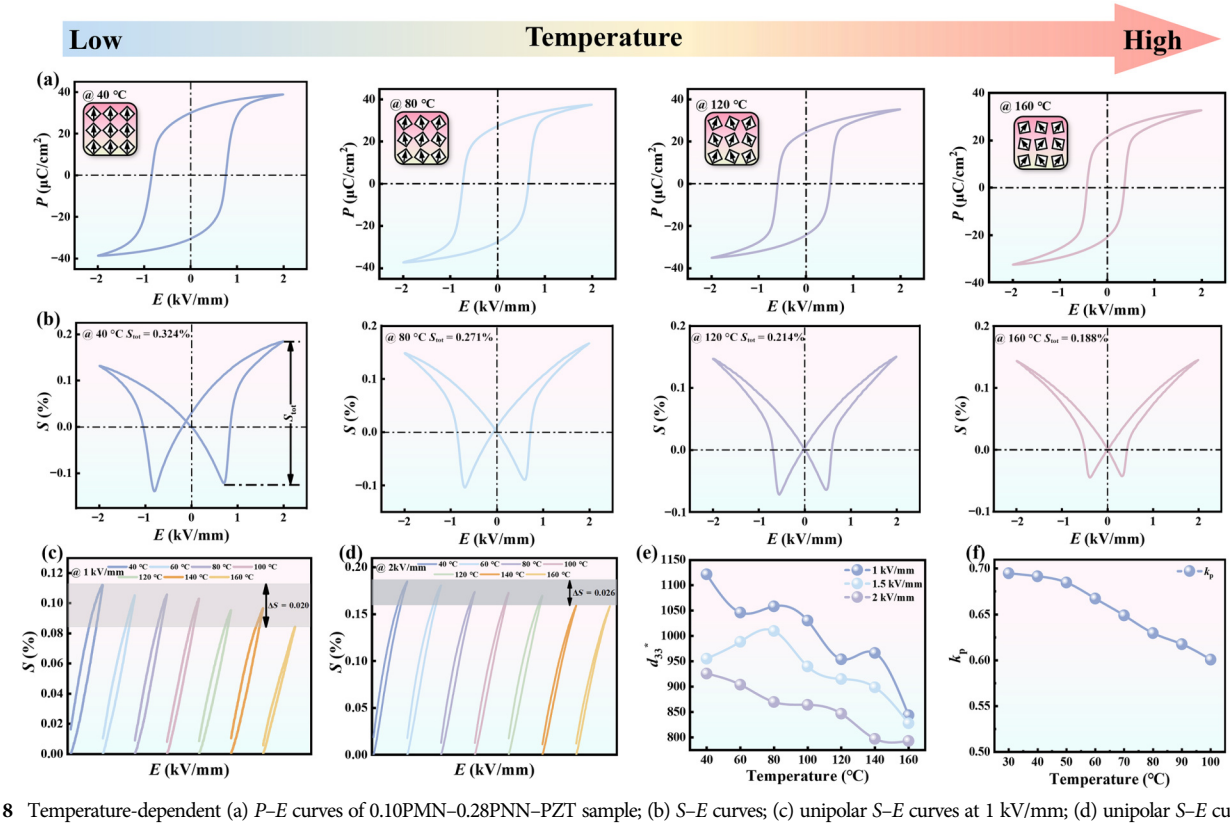


Fig. 8 Temperature-dependent (a) P–E curves of 0.10PMN–0.28PNN–PZT sample; (b) S–E curves; (c) unipolar S–E curves at 1 kV/mm; (d) unipolar S–E curves at 2 kV/mm; (e) summary of d_{33}*–T_C at 1, 1.5, and 2 kV/mm; (f) k_p of 0.15PMN–0.23PNN–PZT sample.

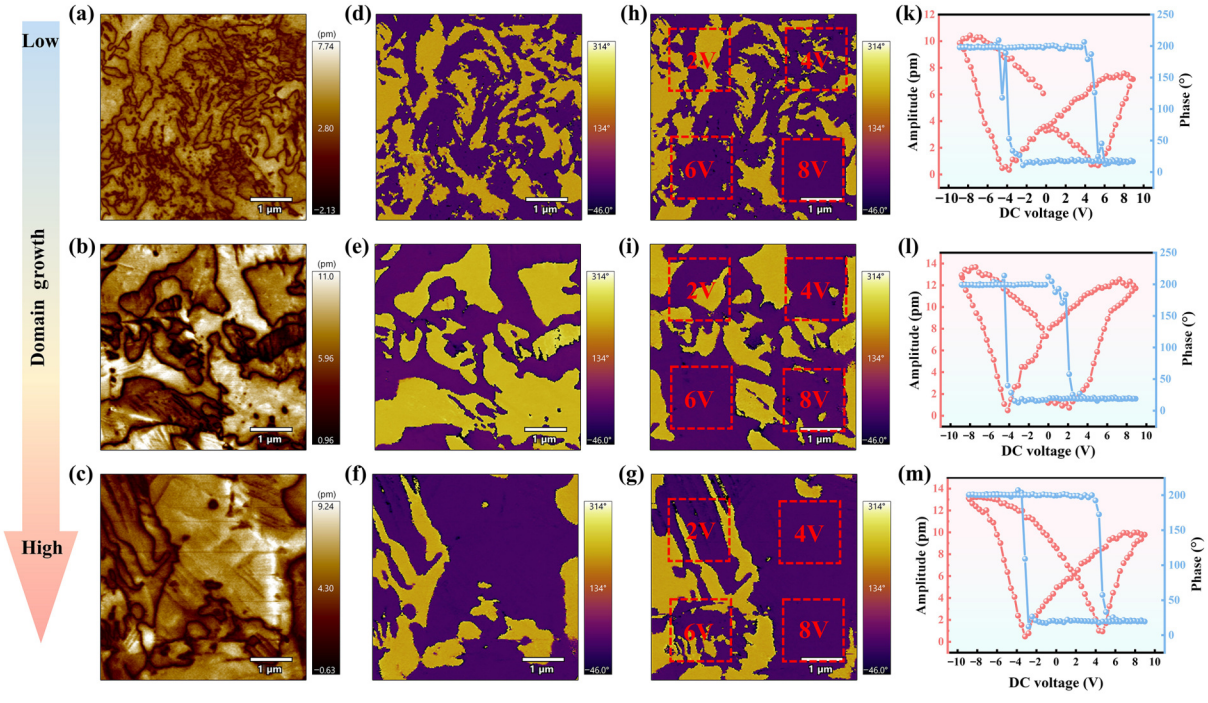


Fig. 9 (a–c) Microarea PFM amplitude images of *x*PMN–(0.38–*x*)PNN–PZT samples (x = 0.00, 0.10, and 0.20); (d–f) phase images at 1.5 Hz; (h–g) domain switching behavior under different voltages; (k–m) amplitude and phase hysteresis loops.

ferroelectric properties. Therefore, the temperature stability of the k_p of the x = 0.15 ceramic sample was also tested, as shown in Fig. 8(f) (Fig. S6(c) in the ESM). Within the temperature range of 100 °C, k_p remains approximately 0.60, comparable to that of the PNN–PZT samples (x = 0.00), indicating that the addition of PMN effectively broadens the working temperature range of the ceramic samples. Thus, the comprehensive evaluation of the temperature-dependent ferroelectric and electrical properties confirms the excellent temperature stability of PMN–PNN–PZT at high temperatures, creating the necessary conditions for its practical applications.

To gain a deeper understanding of the intrinsic mechanisms governing the influence of the ferroelectric domain size on the piezoelectric response of PMN–PNN–PZT ceramics, we further employed microarea PFM to characterize the ferroelectric domains. The microstructure of ferroelectric domains for samples with x = 0.00, 0.10, and 0.20 is shown in Figs. 9(a)–9(c) and 9(d)–9(f). Domains were randomly selected for all samples. Notably, as the PMN content increases, the domain size progressively enlarges. For the x = 0.10 sample, some disorder in the ferroelectric domains is still evident, while for the x = 0.20 sample, the domain size significantly increases, with the appearance of 180° stripe domains. It can be anticipated that such domains require a larger electric field to undergo switching. To further explore the response of ferroelectric domains to the electric field in different ceramic samples, PFM domain writing was performed. As shown in Figs. 9(h)–9(g) (height images, Figs. S2(d)–S2(g) in the ESM), distinct domain switching behaviors were observed under the same voltage for the different samples. Specifically, the x = 0.10 ceramic sample demonstrates rapid domain switching at lower electric fields, with most of the ferroelectric domains flipping easily. In contrast, the smaller domains of the x = 0.00 sample and the larger domains of the x = 0.20 sample show reduced sensitivity to small electric fields, which is reflected in the enhanced piezoelectric performance and lower hysteresis in small field strain for the x = 0.10 sample. Thus, this indicates that promoting domain growth and weakening the domain wall pinning effect facilitates polarization switching, thereby significantly improving the overall performance of the ceramics. However, it is important to note that excessive domain growth can lead to a deterioration of the piezoelectric performance, as shown in the bipolar curves in Figs. 9(k)–9(m).

4 Conclusions

This study introduces a synergistic strategy utilizing PMN to induce lattice distortion and promote ferroelectric domain growth, achieving the concurrent enhancement of d_{33}, d_{33}*, T_C, and k_p in PNN–PZT ceramics while simultaneously reducing the tanδ of the piezoelectric ceramics. When x = 0.10, the ceramic sample exhibits excellent overall performance (d_{33} = 681 pC/N, T_C = 213 °C, k_p = 0.69, d_{33}* = 953 pm/V, H = 14.14% @ 1 kV/mm). This exceptional performance results from the combined enhancement of both intrinsic and extrinsic contributions. Additionally, while promoting ferroelectric domain growth, a certain fraction of small domain structures is retained, which allows the ceramic sample to achieve high sensitivity at both low and high electric fields, as well as excellent temperature stability.

Furthermore, the cooperative strategy of inducing lattice distortion and modulating domain structure through the ionic radius difference of B-site ions holds significant potential for practical applications. By strategically selecting B-site ions with varying radii (such as Zn^{2+}, Mg^{2+}, Ni^{2+}, In^{3+}, or Yb^{3+}) and carefully designing and tailoring multicomponent systems, it is possible to achieve similar synergistic effects. This approach offers a promising solution to the trade-off challenge between competing properties. In conclusion, the successful realization of this strategy presents a simple yet effective paradigm for overcoming the antagonistic relationships commonly encountered in piezoelectric ceramics.

Acknowledgements

This work was supported by the National Key R&D Program of

China (No. 2023YFB3208400), Oil & Gas Major Project (No. 2025ZD1402003), and the National Natural Science Foundation of China (No. U2241242).

Availability of data and materials

The data that support the findings of this study are available from the corresponding author upon reasonable request.

Competing interests

The authors have no competing interests to declare that are relevant to the content of this article.

Electronic Supplementary Material

Supplementary material is available in the online version of this article at https://doi.org/10.26599/JAC.2026.9221294.

References

[1] Li F, Wang B, Gao XY, *et al.* Ferroelectric materials toward next-generation electromechanical technologies. *Science* 2025, **389**: eadn4926.

[2] Li ZM, Yi XY, Yang JK, *et al.* Designing artificial vibration modes of piezoelectric devices using programmable, 3D ordered structure with piezoceramic strain units. *Adv Mater* 2022, **34**: 2107236.

[3] Zheng MP, Hou YD, Yan XD, *et al.* The structural origin of enhanced energy harvesting performance in piezoelectric perovskite. *J Eur Ceram Soc* 2018, **38**: 585–591.

[4] Hao JG, Li W, Zhai JW, *et al.* Progress in high-strain perovskite piezoelectric ceramics. *Mat Sci Eng R* 2019, **135**: 1–57.

[5] Wang L, Qi H, Gao BT, *et al.* Large piezoelectricity in $NaNbO_3$-based lead-free ceramics via tuning oxygen octahedral tilt. *Mater Horiz* 2022, **9**: 1002–1009.

[6] Wu HS, Murti BT, Singh J, *et al.* Prospects of metal-free perovskites for piezoelectric applications. *Adv Sci* 2022, **9**: 2104703.

[7] You YM, Liao WQ, Zhao DW, *et al.* An organic–inorganic perovskite ferroelectric with large piezoelectric response. *Science* 2017, **357**: 306–309.

[8] Strayer ME, Gupta AS, Akamatsu H, *et al.* Emergent noncentrosymmetry and piezoelectricity driven by oxygen octahedral rotations in $n = 2$ Dion–Jacobson phase layer perovskites. *Adv Funct Mater* 2016, **26**: 1930–1937.

[9] Jia FH, Xu SW, Hu SB, *et al.* Understanding the intrinsic piezoelectric anisotropy of tetragonal ABO_3 perovskites through a high-throughput study. *npj Comput Mater* 2025, **11**: 6.

[10] Shi YJ, Dong XY, Zhao KY, *et al.* Potential high-temperature piezoelectric ceramics with remarkable performances enhanced by the second-order Jahn–Teller effect. *ACS Appl Mater Inter* 2021, **13**: 14385–14393.

[11] Nagle-Cocco LAV, Genreith-Schriever AR, Steele JMA, *et al.* Displacive Jahn–Teller transition in $NaNiO_2$. *J Am Chem Soc* 2024, **146**: 29560–29574.

[12] Yun PD, Zhang ML, Chen ZQ, *et al.* Local lattice distortion drives enhanced piezoelectricity and thermal stability in $0.9Pb(Yb,Nb)O_3$–$0.1Pb(Hf,Ti)O_3$ ceramics. *J Alloy Compd* 2025, **1037**: 182455.

[13] Wang SS, Khan AA, Teale S, *et al.* Large piezoelectric response in a Jahn–Teller distorted molecular metal halide. *Nat Commun* 2023, **14**: 1852.

[14] Hong Y, Byeon P, Bak J, *et al.* Local-electrostatics-induced oxygen octahedral distortion in perovskite oxides and insight into the structure of Ruddlesden–Popper phases. *Nat Commun* 2021, **12**: 5527.

[15] Yan YX, Chen ZQ, Yun PD, *et al.* Unraveling the mechanistic discrepancies in properties between rhombohedral and tetragonal PIN–PHT piezoelectric ceramics: Oxygen octahedral distortion as a structural determinant. *Ceram Int* 2025, **51**: 52181–52191.

[16] Tan JH, Huang RX, Dai YJ, *et al.* Improvement of electrostrain properties of BNT-based piezoelectric ceramics by co-doping of Sr^{2+} and Ta^{5+} in A and B sites. *Ceram Int* 2023, **49**: 35399–35405.

[17] Nie R, Yuan J, Chen Q, *et al.* Crystal distortion and electrical properties of Ce-doped BIT-based piezoelectric ceramics. *J Am Ceram Soc* 2019, **102**: 5432–5442.

[18] Ye F, Cheng H, Jiang XP, *et al.* Sn and Ce co-doping regulate phase structure of $NaNbO_3$: Double hysteresis loop and electro-strain. *J Adv Ceram* 2025, **14**: 9221119.

[19] Chen H, Xie YN, Xi JW, *et al.* High piezoelectricity induced by lattice distortion and domain realignment in Li_2CO_3-added lead-based ceramics. *J Mater Chem A* 2023, **11**: 25945–25954.

[20] Finkel P, Cain MG, Mion T, *et al.* Simultaneous large optical and piezoelectric effects induced by domain reconfiguration related to ferroelectric phase transitions. *Adv Mater* 2022, **34**: 2106827.

[21] Zhou MJ, Peng K, Tan YZ, *et al.* Domain evolution, dielectric and piezoelectric response in bent freestanding $PbTiO_3$ ferroelectric nanowires. *Acta Mater* 2025, **288**: 120805.

[22] Song XJ, Xiong YA, Zhou RJ, *et al.* The first demonstration of strain-controlled periodic ferroelectric domains with superior piezoelectric response in molecular materials. *Adv Mater* 2023, **35**: 2211584.

[23] Qiao Y, Wang LL, Zhang DY, *et al.* Effects of heterovalent ions doping-induced oxygen octahedral distortion and defect chemical change on piezoelectric characteristics and thermal stability of PHT–PIN ceramics. *Chem Eng J* 2024, **485**: 150145.

[24] Zhang YK, Chen JW, Yu RZ, *et al.* High-performance piezotronic devices. *ACS Nano* 2025, **19**: 6705–6728.

[25] Liu X, Tang MY, Zhang YL, *et al.* High piezoelectricity and strong field endurance in $Pb(Zr,Ti)O_3$-rich textured ceramics. *Adv Funct Mater* 2026, **36**: e15940.

[26] Li F, Zhang SJ, Xu Z, *et al.* The contributions of polar nanoregions to the dielectric and piezoelectric responses in domain-engineered relaxor-$PbTiO_3$ crystals. *Adv Funct Mater* 2017, **27**: 1700310.

[27] Li F, Lin DB, Chen ZB, *et al.* Ultrahigh piezoelectricity in ferroelectric ceramics by design. *Nat Mater* 2018, **17**: 349–354.

[28] Yan YX, Li ZM, Jin L, *et al.* Extremely high piezoelectric properties in Pb-based ceramics through integrating phase boundary and defect engineering. *ACS Appl Mater Inter* 2021, **13**: 38517–38525.

[29] Lin JM, Liu B, Liu MX, *et al.* Manipulating piezoelectric and electro-strain properties of $BiFeO_3$–$BaTiO_3$-based ceramics through chemical doping-controlled domain-size engineering. *Acta Mater* 2025, **297**: 121379.

[30] Yan L, Yao Y, Wang ZP, *et al.* Gradient-acceptor-doping breaks the piezoelectric trade-off in lead-free (K, Na)NbO_3 ceramics. *Adv Mater* 2026, **38**: 21306.

[31] Tang MJ, Tan Z, Xing J, *et al.* Ultra-high piezoelectric properties and ultra-high Curie temperature of Li/Ce-doped $La_2Ti_2O_7$ ceramics. *Mater Horiz* 2024, **11**: 2898–2905.

[32] Hua Y, Tang LM, Qian J, *et al.* Outstanding comprehensive piezoelectric properties in KNN-based ceramics via co-optimization of crystal structure and grain orientation. *Acta Mater* 2025, **297**: 121378.

[33] Rodríguez-Carvajal J. Recent advances in magnetic structure determination by neutron powder diffraction. *Physica B* 1993, **192**: 55–69.

[34] Ali Khan S, Ahmed T, Park HW, *et al.* Effects of B- and A/B-sites Codoping on lattice distortion and defect concentration for high electromechanical response of lead-free piezoelectrics. *Acta Mater* 2024, **278**: 120262.

[35] Shi HL, Zhao M, Zhang DY, *et al.* Effect of Sb-induced oxygen octahedral distortion on piezoelectric performance and thermal stability of $Pb(In,Nb)O_3$–$Pb(Hf,Ti)O_3$ ceramics. *J Mater Sci Technol* 2023, **161**: 101–110.

[36] Småbråten DR, Holstad TS, Evans DM, *et al.* Domain wall mobility and roughening in doped ferroelectric hexagonal manganites. *Phys Rev Res* 2020, **2**: 033159.

[37] Zhang HY, Chen XG, Tang YY, *et al.* PFM (piezoresponse force microscopy)-aided design for molecular ferroelectrics. *Chem Soc Rev* 2021, **50**: 8248–8278.

[38] Qin Y, Liu WB, Ding Y, *et al.* Enhanced electromechanical response in Dy^{3+}-doped PNN–PZT relaxor ferroelectrics. *Nanoscale* 2025, **17**: 10685–10696.
[39] Peng W, Chang JL, Zhao JW, *et al.* Enhanced piezoelectric properties and thermal stability of $LiNbO_3$-modified PNN–PZT ceramics. *J Materiomics* 2024, **10**: 995–1003.
[40] Yan YX, Qiao Y, Wang LL, *et al.* A novel strategy for obtaining lead-based piezoelectric ceramics with giant piezoelectricity and high-temperature stability through the construction of "slush-like" polar states. *J Mater Sci Technol* 2025, **221**: 25–35.
[41] Feng XY, Xu J, Zhang KN, *et al.* High-sensitivity piezoelectric response enabled by heterogeneous stress–electric field distribution in 3D interconnected porous ceramics. *J Adv Ceram* 2026, **15**: 9221280.
[42] Zhang ZF, Chen L, Luo HJ, *et al.* Outstanding electromechanical performance in piezoelectric ceramics via synergistic effects of defect engineering and domain miniaturization. *J Mater Sci Technol* 2023, **158**: 1–8.
[43] Wang Q, Bian L, He S, *et al.* Morphotropic phase boundary composition PNN–PZT ceramics and their outstanding electromechanical properties. *J Alloy Compd* 2024, **1002**: 175249.
[44] Gao XY, Wu JG, Yu Y, *et al.* Giant piezoelectric coefficients in relaxor piezoelectric ceramic PNN–PZT for vibration energy harvesting. *Adv Funct Mater* 2018, **28**: 1706895.
[45] Zhang J, Zhang YS, Yan ZM, *et al.* Fabrication and performance of PNN–PZT piezoelectric ceramics obtained by low-temperature sintering. *Sci Eng Compos Mater* 2020, **27**: 359–365.
[46] Pu T, Chen H, Xing J, *et al.* High piezoelectricity of low-temperature sintered Li_2CO_3-added PNN–PZT relaxor ferroelectrics. *J Mater Sci—Mater El* 2022, **33**: 4819–4830.
[47] Gao XY, Jin HN, Xin BJ, *et al.* Low temperature sintering of Li_2CO_3 added $Pb(Ni_{1/3}Nb_{2/3})$–$Pb(Zr,Ti)O_3$ ceramics with high piezoelectric properties. *J Alloy Compd* 2022, **892**: 162132.
[48] Peng W, Chang JL, Wang B, *et al.* Ultrahigh piezoelectricity of PNN–PZT ceramics via constructing defect dipoles. *Ceram Int* 2024, **50**: 6598–6605.
[49] Gu CM, Peng W, Shi LZ, *et al.* Superior piezoelectric and mechanical properties in low-temperature sintered PNN–PZT ceramics via compositional design. *Ceram Int* 2025, **51**: 58902–58910.
[50] Wang HL, Zhang FF, Chen Y, *et al.* Giant piezoelectric coefficient of PNN–PZT-based relaxor piezoelectric ceramics by constructing an R–T MPB. *Ceram Int* 2021, **47**: 12284–12291.
[51] Guo FF, Zhang SK, Long W, *et al.* SnO_2 modified PNN–PZT ceramics with ultra-high piezoelectric and dielectric properties. *Ceram Int* 2022, **48**: 23241–23248.
[52] Bian L, Wang Q, Qi XD, *et al.* Improved electromechanical properties of $Pb(Ni_{1/3}Nb_{2/3})O_3$–$PbZrO_3$–$PbTiO_3$ ferroelectric ceramics via Sm-modification. *Ceram Int* 2024, **50**: 5739–5745.
[53] Cheng C, Zheng DY, Peng GG, *et al.* The effects of Sm_2O_3 doping on properties of PNN–PZT ceramics near morphotropic phase boundary. *J Mater Sci—Mater El* 2016, **28**: 1624–1630.
[54] Peng GG, Zheng DY, Cheng C, *et al.* Effect of rare-earth addition on morphotropic phase boundary and relaxation behavior of the PNN–PZT ceramics. *J Alloy Compd* 2017, **693**: 1250–1256.
[55] Liu H, Nie R, Yue Y, *et al.* Effect of MnO_2 doping on piezoelectric, dielectric and ferroelectric properties of PNN–PZT ceramics. *Ceram Int* 2015, **41**: 11359–11364.
[56] Du JZ, Qiu JH, Zhu KJ, *et al.* Effects of Fe_2O_3 doping on the microstructure and piezoelectric properties of $0.55Pb(Ni_{1/3}Nb_{2/3})O_3$–$0.45Pb(Zr_{0.3}Ti_{0.7})O_3$ ceramics. *Mater Lett* 2012, **66**: 153–155.
[57] Du JZ, Qiu L, Xiao X, *et al.* High piezoelectricity in PFN–PNN–PZT quaternary ceramics achieved via composition optimization near morphotropic phase boundary. *Ceram Int* 2022, **48**: 30891–30899.
[58] Wang JJ, Wang SH, Li X, *et al.* High piezoelectricity and low strain hysteresis in PMN–PT-based piezoelectric ceramics. *J Adv Ceram* 2023, **12**: 792–802.
[59] Zhu CX, Qian J, Tang LM, *et al.* Ultra-high energy harvester performance in KNN-based textured piezoceramics via multiscale reconfiguration design. *J Adv Ceram* 2025, **14**: 9221167.
[60] O'Malley CJ, Tang XY, Koval V, *et al.* Unveiling the mechanism of substitution-induced high piezoelectric performance in PLZT ceramics. *J Adv Ceram* 2025, **14**: 9221097.
[61] Chen ZR, Hao YS, Huang J, *et al.* Poling above the Curie temperature driven large enhancement in piezoelectric performance of Mn doped PZT-based piezoceramics. *Nano Energy* 2023, **113**: 108546.
[62] Guo SP, Liang RH, Chen ZR, *et al.* High electric-field-induced strain of SnO_2-modified PLSBZT ceramic for actuator applications. *J Am Ceram Soc* 2024, **107**: 4801–4810.
[63] He RC, Guo HT, Yao ZK, *et al.* Negligible-hysteresis piezoceramic achieved by multiphase assisting and domain configuration manipulating. *J Adv Ceram* 2025, **14**: 9221160.
[64] Li K, Cong S, Bian L, *et al.* Simultaneous enhancement of piezoelectricity and temperature stability in $Pb(Ni_{1/3}Nb_{2/3})O_3$–$PbZrO_3$–$PbTiO_3$ piezoelectric ceramics via Sm-modification. *J Adv Ceram* 2024, **13**: 1578–1589.
[65] Shi HL, Zhang DY, Li ZM, *et al.* Attaining excellent piezoelectric properties and thermal stability in PIN–PHT ceramics by integrating tetragonal phase and relaxor ferroelectrics. *Ceram Int* 2023, **49**: 31784–31793.
[66] Ouyang X, Yao MW, Yang TQ, *et al.* Correlations and mechanisms between temperature stability and structural stability of PNN–PHT piezoceramics. *ACS Appl Mater Inter* 2025, **17**: 10802–10814.